JCTC Journal of Chemical Theory and Computation

Intrinsic Carbon−Carbon Bond Reactivity at the Manganese Center of Oxalate Decarboxylase from Density Functional Theory

Christopher H. Chang[†] and Nigel G. J. Richards*

Department of Chemistry, University of Florida, Gainesville, Florida 32611-7200

Abstract: The detailed manganese-dependent chemistry employed by oxalate decarboxylase (OxDC) to catalyze the nonoxidative decarboxylation of oxalic acid remains poorly understood. For example, enzyme activity requires the presence of dioxygen even though this compound is not a formal substrate in the reaction. We now report density functional theory (DFT) calculations upon a series of hypothetical OxDC active site model structures. Our results suggest that the function of the metal ion may be to position dioxygen and oxalate such that electrons can be shuttled directly between these species, thereby removing the need for the existence of Mn(III) as an intermediate in the mechanism. These calculations also indicate that the intrinsic, gas-phase reactivity of the *Bacillus subtilis* oxalate *decarboxylase* active center is to *oxidize* oxalate. Since this reactivity is not observed for OxDC, our DFT results suggest that protein environment modulates the intrinsic metallocenter reactivity, presumably by affecting the electronic distribution at the manganese center during catalysis.

Introduction

Oxalate decarboxylase (E.C. 4.1.1.2) (OxDC) catalyzes the nonoxidative decarboxylation of oxalic acid to formic acid and carbon dioxide.[1] This transformation is interesting because the enzyme employs manganese to cleave the relatively inert C−C bond in the substrate,[2] although the role of the metal ion in catalysis is poorly understood.[3] A further puzzling observation is that OxDC is inactive under anaerobic conditions even though the decarboxylation is a redox-neutral reaction.[2−4] Chemical precedent for direct homolytic C−C bond cleavage in the breakdown of carboxylic acids is provided by the Kolbe[5] and Hunsdiecker[6] reactions, and similar, radical-dependent mechanisms likely mediate oxalate decomposition in the presence of light and flavins[7] or high-valent Mn species.[8] On the other hand, heavy atom (^{13}C and ^{18}O) isotope effect measurements provide support for a mechanism in which heterolytic bond C−C cleavage takes place in a Mn-bound oxalate radical anion.[9] Studies of the pH dependence of OxDC activity have also established that monoprotonated oxalate is the substrate that initially binds within the OxDC active site.[9] These observations are consistent with a mechanistic model in which the radical anion intermediate and Mn(II) are generated by reversible, proton-coupled electron transfer[10] from Mn(III)-bound, mono-protonated oxalate prior to decarboxylation (Scheme 1). Alternate proposals involving the involvement of higher-valency Mn(IV)-containing intermediates[11] could not, however, be ruled out on the basis of these heavy-atom isotope effect experiments.

Modern density functional theory (DFT) calculations represent an alternative strategy for investigating (i) the likely involvement of high-valent Mn(III) or Mn(IV) species in OxDC-catalyzed oxalate breakdown and (ii) the effects of protonation on the electronic properties of hypothetical OxDC active site model structures corresponding to potential Michaelis complexes and intermediates that might be formed prior to C−C bond cleavage (Scheme 2).[12] In combination with bonding analyses of the Kohn−Sham wave function

* Corresponding author phone: (352)392-3601; e-mail: richards@qtp.ufl.edu.

[†] Present address: National Renewable Energy Laboratory, 1617 Cole Boulevard, Mail Stop 1608, Golden, CO 80401.

Mn-Dependent C−C Bond Cleavage

J. Chem. Theory Comput., Vol. 1, No. 5, 2005 **995**

Scheme 1: Hypothetical Catalytic Mechanism for Oxalate Decarboxylase Based on Heavy-Atom Isotope Effect Studies[9]
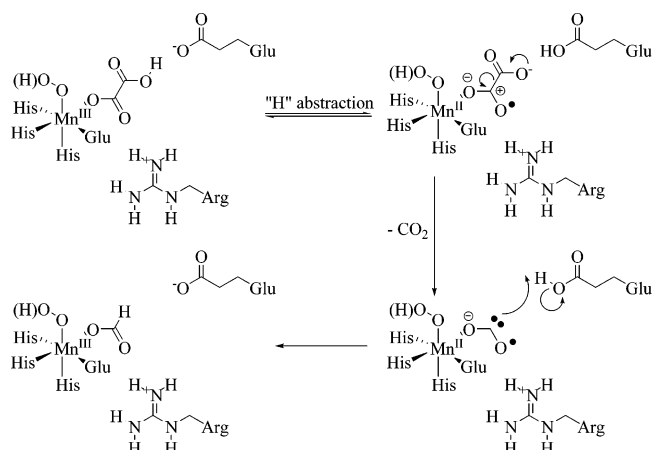

employing the Natural Bond Orbital (NBO) framework,[13] we have employed DFT methods (i) to elucidate the resting valence of the OxDC Mn center in the presence and absence of dioxygen, (ii) to investigate whether formation of superoxide or peroxide can take place in Mn-bound substrate complexes, (iii) to determine the effects of protonating Mn-bound oxalate and dioxygen on metal charge and spin redistribution, and (iv) to identify structures in which the oxalate C−C bond might be weakened significantly. Prior computational studies of the metal centers in Fe- and Mn-dependent enzymes have yielded considerable insights into mechanistic details that are difficult to obtain using current experimental methods.[14,15] The results discussed herein have interesting implications for the general understanding of the mechanistic basis of the decarboxylation and oxidation reactions catalyzed by OxDC and oxalate oxidase (OxOx), respectively, and the role of dioxygen in generating Mn(III) and Mn(IV) complexes for OxDC-catalyzed C−C bond cleavage.

Computational Methods

Construction of Active Site Models 1−14. The initial coordinates for each of the active site model structures were obtained by excising the Mn-bound residues corresponding to His-95, His-97, Glu-101, and His-140 (*Bacillus* subtilis residue numbering) from the crystal structure of OxDC (code: 1J58)[11] deposited in the Protein Data Bank,[16] together with the metal ion and its ligands (water and formate).

The N-terminal site was chosen for the template because (1) formate was bound to the metal despite the absence of this ligand in preparation or crystallization buffers, and (2) oxalate could not be modeled into the C-terminal site of the 1J58 crystal structure without unrealistic steric clashes. This choice is also consistent with recent literature evidence supporting the N-terminal Mn-binding site as the primary site of oxalate breakdown in this enzyme.[17] Backbone atoms of the protein residues, with the exception of the C_α carbon, were then deleted, and hydrogens added to give ethyl-imidazole and butyrate ligands coordinating the metal (Figure 1). The six C−C distances involving the carbon atoms of the capping methyl groups were fixed at their crystallographic values so as to prevent significant distortions of the active site model structures during geometry optimization.[18]

Geometry Optimization of Model Complexes. Spin-unrestricted geometry optimizations of the active site model structures were performed with the TURBOMOLE software package.[19] Calculations upon neutral and cationic complexes used the BLYP exchange-correlation functional[20] with a split-valence + polarization (SVP) double-ζ basis set[21] and employed the "resolution-of-the-identity" approximation for Coulomb integrals (RI).[22] In the case of the anionic complexes (**4**, **5**, and **11**), for which the inclusion of diffuse functions was critical, the lack of a suitable fitting basis for the RI algorithm required standard methods for evaluating Coulomb integrals, and so these calculations employed an SVP basis on H, C, and Mn and a 6-31+G* basis on the O and N centers.[23] DFT calculations on model complexes

Scheme 2: Schematic Overview of the Relationship of the Model Complexes to Steps in the OxDC-Catalyzed Reaction[a]
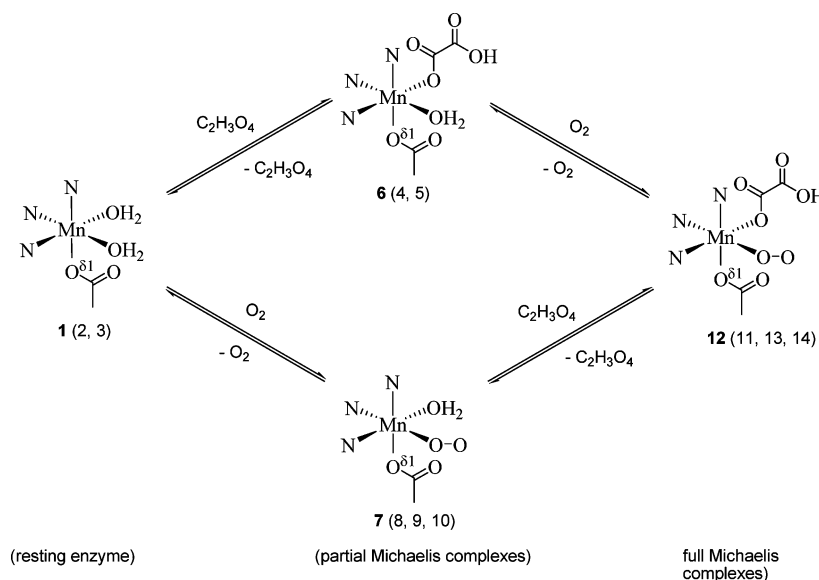
[a] Models that are listed *but not shown explicitly* differ from their parent complex (bold numbers) in the scheme by the loss or addition of protons from/to the water, metal-bound dioxygen or oxalate ligands
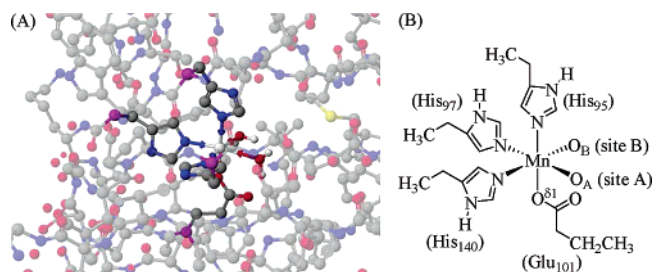
Figure 1. (A) Visualization of the putative, N-terminal active site in the crystal structure of *Bacillus subtilis* OxDC,[11] with the observed Mn-bound formate replaced by a water molecule to give the H_2O-H_2O complex **1**. Highlighted atoms represent those used to construct active site models **1−14**. The purple atoms correspond to the α-carbons that are transformed into methyl groups in the model complexes. The relative coordinates of the purple atoms were fixed during geometry optimization. The more solvent accessible coordination site (site B), to which oxalate is assumed to bind in these studies, faces away from the reader and toward a selenomethionine residue. With the exception of the two Mn-bound water molecules, only non-hydrogen atoms are shown for clarity. Atoms are colored using the following scheme: C, gray; H, white; N, blue; O, red; Se, yellow; Mn, white. (B) Schematic representation of model complexes **1−14** showing the location of sites A and B relative to the ethylimidazole and butyrate moieties corresponding to the protein residues that coordinate manganese.

containing Mn-bound dioxygen (**7−14**) were performed at both $M_S = 3/2$ and $M_S = 5/2$ spin configurations, while all other calculations assumed that Mn was present in its high-spin $M_S = 5/2$ electronic configuration for reasons that are described below. Geometry optimizations were converged to 10^{-6} Ha in total energy and 10^{-3} Ha/Bohr in the Cartesian gradients, unless bond cleavage took place in which case the calculation was terminated since one or more dimensions on the potential surface became essentially flat. Unrestricted B3LYP[24] optimizations on active site models **11−14** were also undertaken to examine the effects of including exact exchange and employed an SVP(+) basis.

NBO Analysis of the Kohn−Sham Wave Functions. The Kohn−Sham wave functions determined for the optimized complexes were analyzed within the Natural Bond Orbital formalism,[13] using the NBO 5.0 package. Input files for this analysis were obtained by performing single point energy calculations for each of the active site models at its optimized geometry using a PBE/LACVP(O/N+)** model chemistry, as implemented in Jaguar V5.0 (Schrödinger LLC, Portland OR). Thus, an effective core potential was used on Mn[27] together with a 6-31G** basis on H, C, and Mn and a 6-31+G** basis on the O and N centers. The extent of covalency in metal−ligand bonds was evaluated using a procedure developed previously for open-shell transition metal complexes,[28] with the modification that 3-centered, 4-electron hyperbonding was accounted for implicitly by analysis of the Natural Localized Molecular Orbitals[29] and Natural Bond Orbitals. Atomic charges and populations were derived from the Natural Population Analysis.[30]

Results and Discussion

Structural Properties and NBO Analysis of Complexes 1−3 (Resting Enzyme). The polypeptide framework of *Bacillus subtilis* OxDC provides residues (His-95, His-97, His-140, and Glu-101) that occupy four of the six Mn-coordination sites in the N-terminal, Mn-binding site.[11] In the original crystal structure of the enzyme, the two remaining coordination sites were occupied by a water molecule (site A) and formate (site B).[11] The latter site appears to be more exposed to bulk solvent in this high-resolution structure, consistent with the hypothesis that Mn-bound oxalate is decarboxylated to yield formate. We therefore assumed in constructing our active site model complexes that (i) the less solvent-accessible and more hydrophobic site A may be occupied by water, hydroxide, or dioxygen derivatives, and (ii) the more solvent-accessible site B may be occupied by water, hydroxide, formate, or mono- or diprotonated oxalate (Figure 1). In our initial calculations, we examined the BLYP-optimized structure and chemical bonding of complexes that model the OxDC Mn-center in the resting enzyme, which could be derived by replacing formate by a water molecule (Figure 1). There were four possible active site complexes due to the two unique binding sites, which we represented as H_2O-H_2O **1**, H_2O-HO^- **2**, HO^--H_2O **3**, and HO^--HO^-. In this notation (Figure 1B), the initial ligand is assumed to occupy coordination site A and the second is therefore located in the more solvent accessible site B. Calculations on the complex containing two Mn-bound hydroxide ligands were not performed, however, given that this species is unlikely to be relevant to any catalytic mechanism given that the enzyme exhibits optimum activity under acidic conditions.[4,9] In addition, only the $M_S = 5/2$ spin configuration was considered for these resting-state model complexes because (i) experimental EPR measurements indicate that the d^5 high-spin state of Mn(II) is the ground state of the resting enzyme,[2a,3b] and (ii) histidine, glutamate, water and hydroxide anion are all weak field ligands.

The geometries of model complexes **1−3** were optimized using the BLYP exchange-correlation functional and a double-ζ SVP basis (Table 1), in part to obtain reference structures that could be used to assess the effects of oxalate and/or dioxygen binding on metal−ligand bonding, molecular geometry, and the spin preferences of the Mn center. These calculations showed that replacing a water by an anionic hydroxide ligand (i) shortened the Mn−O bond length for this ligand, (ii) systematically lengthened the metal−imidazole bonds by approximately 0.1 Å while leaving the Mn−carboxylate distance little changed, and (iii) decreased the N−Mn−N bond angles in almost all of the active site model structures (Table 1). In addition, the angle between the hydroxyl and carboxylate ligands was increased with a concomitant decrease in the water/carboxylate angle. These changes are consistent with those expected due to the increased negative charge of the metal-bound ligand after deprotonation.

To obtain a picture of the chemical bonding in active site model structures **1−3**, we undertook a detailed analysis of the PBE wave function, as represented by a single determi-

Table 1. Selected Structural Properties of BLYP-Optimized Geometries for OxDC Active Site Models **1−3**[a]

internal coordinate[b,c]	H_2O−H_2O **1**	H_2O−HO^- **2**	HO^-−H_2O **3**
Mn−H95N$^\epsilon$	2.279	2.345	2.356
Mn−H97N$^\epsilon$	2.245	2.342	2.326
Mn−E101O$^{\delta 1}$	2.161	2.158	2.174
Mn−H140N$^\epsilon$	2.258	2.369	2.329
Mn−O$_A$	2.307	2.400	2.051
Mn−O$_B$	2.345	2.053	2.452
H95N$^\epsilon$−Mn−H97N$^\epsilon$	92.4	87.14	92.15
H95N$^\epsilon$−Mn−E101O$^{\delta 1}$	176.4	169.1	176.8
H95N$^\epsilon$−Mn−H140N$^\epsilon$	90.84	84.03	85.05
H95N$^\epsilon$−Mn−O$_A$	98.84	95.12	85.31
H95N$^\epsilon$−Mn−O$_B$	85.07	83.57	100.4
H97N$^\epsilon$−Mn−E101O$^{\delta 1}$	85.21	84.02	85.12
H97N$^\epsilon$−Mn−H140N$^\epsilon$	102.1	93.08	95.98
H97N$^\epsilon$−Mn−O$_A$	161.8	175.2	165.1
H97N$^\epsilon$−Mn−O$_B$	100.3	113.1	96.50
E101O$^{\delta 1}$−Mn−H140N$^\epsilon$	92.25	90.06	93.47
E101O$^{\delta 1}$−Mn−O$_A$	82.88	93.24	97.77
E101O$^{\delta 1}$−Mn−O$_B$	92.76	105.8	81.70
H140N$^\epsilon$−Mn−O$_A$	91.99	82.96	98.45
H140N$^\epsilon$−Mn−O$_B$	157.3	150.3	166.2
O$_A$-Mn−O$_B$	66.73	71.46	69.59

[a] All calculations are for the $S = 5/2$ spin state of Mn(II) and are spin-unrestricted. [b] All bond distances and angles are reported in units of Å and deg, respectively. [c] O$_A$ and O$_B$ correspond to the ligating oxygen atoms in the buried (site A) and solvent-exposed (site B) coordination sites (Figure 1), respectively, and O$^{\delta 1}$ is the oxygen of the butyrate moiety corresponding to the Glu-101 residue that is bonded directly to the metal.

nant of canonical Kohn−Sham orbitals, within the NBO formalism for each structure at its ground-state, BLYP-optimized geometry. More specifically, we sought to obtain (i) the distribution of electrons in these complexes, as determined by spin magnetization density (SMD) and partial charges obtained using Natural Population Analysis (NPA),[13,28] (ii) the extent to which our results were subject to spin contamination (Table 2),[14c] and (iii) the extent of metal−ligand bond covalency (Table 3). For all three models of the OxDC center in the resting enzyme (**1−3**), the bonding appeared characteristic of a typical, high-spin Mn(II) complex in that the difference in α- and β-spin density on the metal center was 4.7, and the total *d*-orbital population on Mn was approximately 5.3 electrons, consistent with the metal ion having a d^5 configuration in the $M_S = 5/2$ spin state (Table 2). We also observed that the NPA charges on Mn were unaffected by the presence or absence of hydroxide ion, having a value of approximately +1.4, and that there was some delocalization of ligand β-spin density onto the metal with a corresponding, slight spin polarization of the ligands. More variation was seen in the total metal−ligand covalencies computed for the three active site models **1−3** (Table 3). For example, when hydroxide was present in site A (model **3**), the covalency was significantly higher than that computed for the other two complexes. This increase did not appear correlated with Mn−hydroxide binding, however, but with the covalency of the bonds involving Mn and the ligands modeling the side chains of residues His-95, His-97, and Glu-101. In addition, a decreased covalency in the

metal−ligand bond involving the ethylimidazole corresponding to the His-140 side chain was observed in both of the models containing a hydroxide ligand (**2** and **3**), consistent with our finding that this ligand dissociates from the metal when the geometry of the anionic complex containing two hydroxide ions is optimized.

Structural Properties and NBO Analysis of Complexes 4−6 (Oxalate-Bound Enzyme). Having analyzed the structural models corresponding to the Mn-center in the resting enzyme, we next examined three models (**4−6**) in which oxalate occupies a coordination site (site B) on the metal in the absence of dioxygen (Figure 1B). Geometry optimization, within the RI approximation, of an active site model (**4**) containing the monoprotonated form of oxalate in which the sixth ligand was a hydroxide anion, merely led to dissociation of the ethylimidazole ligands corresponding to His-95 and His-140 in the putative OxDC active site. We therefore performed a similar calculation using a BLYP/SVP(O/N 6-31+G*) model chemistry to account for potentially diffuse electron density in this anionic complex. Even with this expanded basis, geometry optimization still resulted in dissociation of an ethylimidazole ligand (His-140 in OxDC) (Table 4). Similar observations were made for the anionic, oxalate-containing, H_2O−Ox model **5** in that cleavage of the Mn−N bond involving the ethylimidazole corresponding to His-140 took place. The physical and/or mechanistic significance of these results is unclear, however, since the tendency of the Mn−ligand bond to undergo cleavage in these active site models may (i) reflect a change in metal coordination that actually takes place on substrate binding or (ii) be a consequence of neglecting residues defining the protein environment about the metal center in OxDC in our calculations.

On the other hand, it seems unlikely that hydroxide would occupy the sixth coordination site in preference to water in any OxDC/oxalate complex over the pH range of 3.8−5.0 at which OxDC exhibits significant activity.[9] Additional support for this assumption is provided by the measured pK_1 and pK_2 values of free Mn(H_2O)$_6$$^{2+}$, which are estimated to be 10.4 and 22, respectively.[31,32] Thus, the Mn-bound water molecule seems likely to have a pK_a of greater than 20 when oxalate monoanion is also coordinated to the metal. This pK_a may be increased further by the glutamate ligand that coordinates manganese. Efforts to obtain an optimized structure for a model structure in which hydroxide and oxalate dianion occupied coordination sites A and B, respectively, also gave results that were dependent on the model chemistry used in the calculations.[33] Although oxalate dianion might conceivably adopt bidentate coordination at the mononuclear manganese center similar to that recently seen in a putative oxalate decarboxylase from *Thermatoga maritima*,[34] we did not observe such a binding mode in this series of calculations. This may, however, reflect the lack of a suitable proton donor in our active site model containing dianionic oxalate and/or the energy of a free vs bound hydroxide ion in the absence of a solvation potential, and, therefore, participation of bidentate binding in the OxDC active site is not definitively ruled out by this computational investigation.

Table 2. NPA-Derived Partial Charges and Spin Magnetization Densities (SMD) of Selected Atoms in Complexes **1**−**14** at Their DFT-Optimized Geometries[a]

		net charge	$\langle S^2\rangle_{KS}$[b]	partial charge (Mn)	partial charge (O_A)[c]	partial charge (O_C)[c]	SMD (Mn)	SMD (O_A)	SMD (O_C)	SMD (oxalate)[d]	C−C bond order
H_2O−H_2O **1**	$M_S = 5/2$	+1	8.75	+1.44	f	f	4.70	f	f	g	g
H_2O−HO^- **2**	$M_S = 5/2$	0	8.75	+1.38	f	f	4.67	f	f	g	g
HO^-−H_2O **3**	$M_S = 5/2$	0	8.75	+1.39	f	f	4.66	f	f	g	g
HO^-−OxH **4**	$M_S = 5/2$	−1	8.76	+1.48	f	f	4.65	f	f	0.06[e]	0.826
H_2O−Ox **5**	$M_S = 5/2$	−1	8.76	+1.46	f	f	4.62	f	f	0.16[e]	0.874
H_2O−OxH **6**	$M_S = 5/2$	0	8.75	+1.45	f	f	4.68	f	f	0.08[e]	0.928
O_2−H_2O **7**	$M_S = 5/2$	+1	8.92	+1.39	−0.22	−0.16	3.95	0.33	0.46	g	g
O_2−HO^- **8**	$M_S = 5/2$	0	8.84	+1.35	−0.28	−0.22	3.77	0.42	0.52	g	g
HO_2−H_2O **9**	$M_S = 3/2$	+2	3.84	+1.13	−0.25	−0.41	2.76	0.14	−0.01	g	g
HO_2−HO^- **10**	$M_S = 3/2$	+1	3.82	+1.12	−0.28	−0.43	2.68	0.10	0.00	g	g
O_2−Ox **11**	$M_S = 5/2$	−1	9.21	+1.48	−0.29	−0.19	4.26	0.31	0.44	0.25	0.824
O_2−OxH **12**	$M_S = 5/2$	0	9.07	+1.41	−0.21	−0.07	4.10	0.20	0.36	0.12	0.861
HO_2−Ox **13**	$M_S = 5/2$	0	8.76	+1.34	−0.61	−0.58	4.56	0.18	0.06	0.00	0.001
HO_2−OxH **14a**	$M_S = 3/2$	+1	3.86	+1.15	−0.28	−0.54	2.80	0.11	−0.02	0.12	0.912
HO_2−OxH **14b**	$M_S = 5/2$	+1	8.95	+1.40	−0.21	−0.54	3.99	0.29	0.43	0.10	0.908

[a] Complexes are named as discussed in the text and shown in Figure 1B. [b] Noninteracting values of $\langle S^2\rangle_{KS}$ were computed from a single determinant of Kohn−Sham orbitals, using the algorithm implemented in Gaussian98. [c] O_A and O_C correspond to the atoms in the dioxygen or hydroperoxy ligand in the buried coordination site (site A). O_A is bonded to the Mn center. [d] This value was computed using $\Sigma\rho_{\alpha-\beta}$ where the difference in α and β spin densities is summed over all the atoms in the oxalate ligand, including hydrogens when present. [e] Spin polarization on the oxalate moiety in complexes **4**−**6** is associated with the oxygen atom covalently bonded to the Mn center. [f] Not applicable since dioxygen or hydroperoxide is not present in the complex. [g] Not applicable since oxalate is not present in the complex.

Table 3. Calculated Covalent Character of Mn−Ligand Bonds in Complexes **1**−**3** at Their BLYP-Optimized Ground-State Geometries[a]

bond	bond covalency ($|e^-|$)	total covalency ($|e^-|$)
	H_2O−H_2O **1**	
Mn−$H95N^\epsilon$	0.100	0.536
Mn−$H97N^\epsilon$	0.106	
Mn−$E101O^{\delta 1}$	0.101	
Mn−$H140N^\epsilon$	0.097	
Mn−O_A	0.066	
Mn−O_B	0.066	
	H_2O−HO^- **2**	
Mn−$H95N^\epsilon$	0.060	0.603
Mn−$H97N^\epsilon$	0.073	
Mn−$E101O^{\delta 1}$	0.121	
Mn−$H140N^\epsilon$	0.065	
Mn−O_A	0.080	
Mn−O_B	0.204	
	HO^-−H_2O **3**	
Mn−$H95N^\epsilon$	0.196	0.868
Mn−$H97N^\epsilon$	0.214	
Mn−$E101O^{\delta 1}$	0.137	
Mn−$H140N^\epsilon$	0.053	
Mn−O_A	0.197	
Mn−O_B	0.071	

[a] Atom labels correspond to those used in Table 1.

Examination of the chemical bonding in complexes **4**−**6** showed that the NPA charges, spin magnetization densities, and *d*-orbital populations on the Mn center were very similar to those computed for the active site structures modeling the resting state of the enzyme (Table 2). Unlike complexes **1**−**3**, however, substantially increased covalent bonding to Mn in the 5-coordinate complexes resulting from dissociation of the His-140 ligand during geometry optimization was not observed (Table 5). Instead, the oxalate C−C NPA/NLMO

bond order was reduced in models **4** and **5** relative to that in the 6-coordinate active site model **6** (Table 2). This reduction in C−C bond order was mitigated in **5**, however, by hydrogen bonding of the oxalate moiety to the Mn-bound water molecule, which also formed a hydrogen bond to the distal oxygen on the butyrate moiety corresponding to Glu-101 in the enzyme. We therefore interpret the reduced oxalate C−C bond order in this structure to arise from an inductive effect that is enhanced by the loss of His-140 imidazole during geometry optimization. A possible interpretation of these results is that electrostatic polarization alone can weaken the oxalate C−C bond when this substrate becomes bound to the Mn center in OxDC. In addition, hydrogen bonding effects and/or protonation of the distal carboxylate of Mn-bound, monodentate oxalate may operate to modulate the effects of charge polarization so as to create an exquisitely controlled switch,[9] as discussed below.

Structural Properties and NBO Analysis of Complexes 7−10 (Dioxygen-Bound Enzyme). Although OxDC activity is observed only under aerobic conditions, the mechanistic role of dioxygen in catalyzing the decarboxylation of oxalate has yet to be defined unambiguously. We,[9] and others,[2,11] have speculated that dioxygen is employed in the oxidation of Mn(II) to Mn(III) or Mn(IV), which are species that can participate in proton-coupled electron transfer to yield a metal-bound oxalate radical anion (Scheme 1). Recent EPR studies aimed at observing any interaction between Mn(II) and dioxygen under steady-state conditions, however, yielded little direct evidence to support this mechanistic proposal,[3b] although recent work has suggested that dioxygen can bind to Mn(II) if there is sufficient anionic character present in the ligand field.[35] Such behavior can be rationalized in terms of a requirement for formal electron transfer from Mn(II) to dioxygen, thereby yielding a complex that is best described as involving a superoxide anion bound to Mn(III), at least

Mn-Dependent C−C Bond Cleavage

J. Chem. Theory Comput., Vol. 1, No. 5, 2005 **999**

Table 4. Selected Structural Properties of BLYP-Optimized Geometries for OxDC Active Site Models **4**−**6**[a]

internal coordinate[b,c]	HO⁻−OxH **4**	H₂O−Ox **5**	H₂O−OxH **6**
Mn−H95N$^\epsilon$	2.430	2.289	2.372
Mn−H97N$^\epsilon$	2.303	2.346	2.338
Mn−E101O$^{\delta 1}$	2.176	2.119	2.205
Mn−H140N$^\epsilon$	d	d	2.358
Mn−O$_A$	2.013	2.226	2.207
Mn−O$_B$	2.142	1.992	2.108
C$_A$−C$_B$	1.553	1.566	1.550
H95N$^\epsilon$−Mn−H97N$^\epsilon$	87.94	85.22	86.35
H95N$^\epsilon$−Mn−E101O$^{\delta 1}$	164.0	142.3	165.3
H95N$^\epsilon$−Mn−H140N$^\epsilon$	d	d	85.06
H95N$^\epsilon$−Mn−O$_A$	81.24	85.71	101.5
H95N$^\epsilon$−Mn−O$_B$	90.42	96.79	88.21
H97N$^\epsilon$−Mn−E101O$^{\delta 1}$	82.66	80.09	82.18
H97N$^\epsilon$−Mn−H140N$^\epsilon$	d	d	92.26
H97N$^\epsilon$−Mn−O$_A$	130.8	144.0	170.4
H97N$^\epsilon$−Mn−O$_B$	101.2	107.0	95.20
E101O$^{\delta 1}$−Mn−H140N$^\epsilon$	d	d	86.17
E101O$^{\delta 1}$−Mn−O$_A$	95.17	86.15	89.13
E101O$^{\delta 1}$−Mn−O$_B$	104.0	120.7	102.0
H140N$^\epsilon$−Mn−O$_A$	d	d	82.99
H140N$^\epsilon$−Mn−O$_B$	d	d	169.6
O$_A$−Mn−O$_B$	126.5	108.7	90.64
O$_B$−C$_A$−O$_D$	130.4	123.6	128.9
O$_E$−C$_B$−O$_F$	121.5	127.2	121.7

[a] All calculations are for the $S = 5/2$ spin state of Mn(II) and are spin-unrestricted. [b] All bond distances and angles are reported in units of Å and deg, respectively. [c] O$_A$ and O$_B$ correspond to the ligating oxygen atoms in the buried (site A) and solvent-exposed (site B) coordination sites (Figure 1), respectively, and O$^{\delta 1}$ is the oxygen of the butyrate moiety corresponding to the Glu-101 residue that is bonded directly to the metal. C$_A$ and O$_D$ are the remaining atoms in the carboxylate coordinated directly to Mn, and atoms in the other carboxyl moiety in oxalate are defined as C$_B$, O$_E$, and O$_F$. [d] Internal coordinates involving for the ethylimidazole moiety corresponding to His-140 are not presented because this ligand dissociated from the metal during geometry optimization.

Table 5. Calculated Covalent Character of Mn−Ligand Bonds in Complexes **4**−**6** at Their BLYP-Optimized Ground-State Geometries[a]

bond	bond covalency ($|e^-|$)	total covalency ($|e^-|$)
	HO⁻−OxH **4**	
Mn−H95N$^\epsilon$	0.056	0.526
Mn−H97N$^\epsilon$	0.076	
Mn−E101O$^{\delta 1}$	0.102	
Mn−H140N$^\epsilon$	0.001[b]	
Mn−O$_A$	0.209	
Mn−O$_B$	0.082	
	H₂O−Ox **5**	
Mn−H95N$^\epsilon$	0.086	0.495
Mn−H97N$^\epsilon$	0.068	
Mn−E101O$^{\delta 1}$	0.107	
Mn−H140N$^\epsilon$	0.000[b]	
Mn−O$_A$	0.090	
Mn−O$_B$	0.144	
	H₂O−OxH **6**	
Mn−H95N$^\epsilon$	0.075	0.541
Mn−H97N$^\epsilon$	0.071	
Mn−E101O$^{\delta 1}$	0.094	
Mn−H140N$^\epsilon$	0.070	
Mn−O$_A$	0.110	
Mn−O$_B$	0.121	

[a] Atom labels correspond to those used in Table 4. [b] The ethyl-imidazole ligand corresponding to His-140 dissociated from the metal during geometry optimization of this complex.

within a standard ligand field model. Support for such an idea is provided by studies on copper-dependent amine oxidases.[36] The interaction of dioxygen with the Mn(II) center in our active site models was therefore investigated, although these DFT calculations were complicated by the need to consider the effects of spin coupling between triplet O₂ and the metal. Three possible systems can be envisaged in which $S = 3/2$, 5/2, or 7/2. For the case in which $S = 7/2$, the Mn(II)/dioxygen interaction might take place by (i) mixing a formally empty $4s$ orbital on the metal with a filled π MO on the ligand, (ii) mixing of one (or more) half-filled Mn $3d$ orbital(s) with the low-lying half-filled π^* MOs on dioxygen, or (iii) one-electron oxidation of histidyl or glutamyl ligand by dioxygen to give the corresponding radical and superoxide radical anion, resulting in a system containing seven unpaired electrons. Of these possibilities, the first is unlikely, and the second is disfavored because it would require a spin flip (within the standard single determinantal model in which excess unpaired electrons are α-spin) to satisfy the Pauli exclusion principle and permit electron transfer from the Mn d manifold to the O₂ π^* MOs.[37] In addition, while ligand oxidation is observed for thiolates[38]

and high-valent ferryl heme intermediates,[39] such a process seems unlikely for the histidine and glutamate ligands coordinating Mn(II) in the OxDC active site. We therefore focused our computational studies on dioxygen-containing systems for which the total spin corresponded to $S = 3/2$ and $S = 5/2$ and obtained optimized structures for each of the four possible dioxygen-containing active site models **7**−**10** at both of these spin states (Table 6). The use of this single determinantal method to describe open-shell transition metal complexes, which are best described by multiple configurations, is fraught with difficulties.[14c,40] For example, such calculations may yield wave functions exhibiting significant spin contamination, complicating any interpretation of their electronic structure and/or energetics.

In the case of DFT calculations, spin contamination manifests itself as unpaired β-spin density resulting in a value of $\langle S^2 \rangle_{\text{KS}}$ (at least to the degree that this two-electron quantity can be computed from a determinant of Kohn−Sham orbitals[41]) that is larger than $M_S(M_S + 1)$.[15a] We note that methods have been devised to extract reasonable spin-state energies from such broken-symmetry solutions[42] and applied in studies of Fe−S clusters for which spin coupling and valence delocalization patterns have been well characterized by experimental methods, including Mössbauer spectroscopy.[43] Although such methodology might have been employed to examine active site models **7**−**10**, a conceptual parsing of valence and spin subsystems, together with quantitation of the resonance and exchange interactions between them, remains to be established for Mn−O₂ systems. We therefore chose to examine the properties of the lowest energy, DFT-optimized structure for each *only* if it exhibited

1000 *J. Chem. Theory Comput., Vol. 1, No. 5, 2005*

Chang and Richards

Table 6. Selected Structural Properties of BLYP-Optimized Geometries for OxDC Active Site Models **7−10**[a]

internal coordinate[b,c]	O_2-H_2O **7** $M_S = 5/2$	O_2-HO^- **8** $M_S = 5/2$	HO_2-H_2O **9** $M_S = 3/2$	HO_2-HO^- **10** $M_S = 3/2$
$Mn-H95N^\epsilon$	2.141	2.406	2.073	2.112
$Mn-H97N^\epsilon$	2.146	2.555	2.106	2.148
$Mn-E101O^{\delta1}$	1.918	2.079	1.941	1.960
$Mn-H140N^\epsilon$	2.256	2.132	2.005	2.125
$Mn-O_A$	**2.068**[d]	**2.122**	**1.859**	**1.851**
$Mn-O_B$	2.330	1.818	2.033	1.804
O_A-O_C	**1.301**	**1.313**	**1.415**	**1.424**
$H95N^\epsilon-Mn-H97N^\epsilon$	90.18	74.82	91.22	87.55
$H95N^\epsilon-Mn-E101O^{\delta1}$	170.67	147.6	175.5	170.7
$H95N^\epsilon-Mn-H140N^\epsilon$	89.65	85.68	88.14	87.92
$H95N^\epsilon-Mn-O_A$	86.82	77.25	87.16	90.31
$H95N^\epsilon-Mn-O_B$	85.89	90.92	90.50	90.60
$H97N^\epsilon-Mn-E101O^{\delta1}$	88.23	73.95	85.58	85.89
$H97N^\epsilon-Mn-H140N^\epsilon$	98.19	95.39	99.25	93.72
$H97N^\epsilon-Mn-O_A$	173.7	151.9	169.8	177.8
$H97N^\epsilon-Mn-O_B$	93.40	91.04	87.35	89.44
$E101O^{\delta1}-Mn-H140N^\epsilon$	99.68	88.79	89.25	85.99
$E101O^{\delta1}-Mn-O_A$	93.83	134.2	96.55	96.27
$E101O^{\delta1}-Mn-O_B$	85.02	98.09	92.51	95.87
$H140N^\epsilon-Mn-O_A$	87.39	85.90	90.77	86.45
$H140N^\epsilon-Mn-O_B$	167.6	171.7	173.3	176.4
O_A-Mn-O_B	80.82	85.94	82.60	90.33
$Mn-O_B-O_C$	119.1	117.5	117.5	117.2

[a] All calculations are spin-unrestricted. M_S is the sum of the Mn and dioxygen spin states. [b] All bond distances and angles are reported in units of Å and deg, respectively. [c] O_A and O_B correspond to the ligating oxygen atoms in the buried (site A) and solvent-exposed (site B) coordination sites (Figure 1), respectively, and $O^{\delta1}$ is the oxygen of the butyrate moiety corresponding to the Glu-101 residue that is bonded directly to the metal. O_C is the atom in the dioxygen ligand that is not bound to Mn. [d] Highlighted internal coordinates are discussed explicitly in the text.

insignificant amounts of spin contamination as computed from $\langle S^2 \rangle_{KS}$.[15a] For active site structures containing protonated (**9** and **10**) and unprotonated dioxygen (**7** and **8**), these criteria were met by systems for which $S = 3/2$ and $S = 5/2$, respectively.

The structural properties of these DFT-optimized active site models were consistent with qualitative expectations based on ligand field theory (Table 6). For example, hydroxide was bound more tightly to the metal center than water in these four active site models (**7−10**), and the O−O bond length (O_A-O_C) in the dioxygen moiety was correlated with its protonation state. Thus, there was a lengthening of the O_A-O_C bond with a concomitant decrease in the metal− ligand bond ($Mn-O_A$) when a proton was attached to the distal oxygen (Table 6), suggesting that protonation enhances the extent of metal to ligand charge transfer in these complexes. We also note that binding dioxygen and hydroxide in the nonproteinaceous coordination sites A and B, respectively, causes an increase in the bond lengths between the metal and the ligands corresponding to OxDC residues His95, His97, and Glu101 relative to the cognate geometric parameters in the other three complexes (Figure 2). This effect may be associated with the uncompensated negative charge in the hydroxide-bound model **8**. Similar, albeit
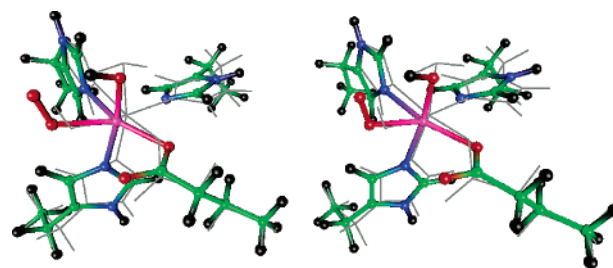
Figure 2. Stereoscopic image (cross-eyed) showing the superposition of the BLYP-optimized structures of the O_2- H_2O (**7**) and the O_2-HO^- (**8**) active site model complexes. Structures are rendered according to the following scheme: (**8**) C, green; H, black; N, blue; O, red; Mn, magenta; (**7**) gray.

smaller, changes in metal−dioxygen bond length are observed for complexes **9** and **10** in which this ligand is protonated. Thus, protonation of dioxygen appears to drive electron density from the metal center, and the ensuing partial reduction of the HO_2 ligand is therefore facilitated by the presence of the negatively charged hydroxide anion. Spin coupling to give complexes with net $S = 3/2$ or $S = 5/2$ spin states permits either metal-to-ligand charge donation or outright electron transfer between Mn(II) and dioxygen to yield an active site model that can be formally described as a superoxide-Mn(III) species, as proposed in previous mechanistic hypotheses.[2,9]

For the two complexes **7** and **8**, in which hydroxide or water was present in the "oxalate-coordination" site, the final DFT wave functions for these optimized structures exhibited little spin contamination, based on the $\langle S^2 \rangle_{KS}$ values of 8.8 and 8.9 (Table 2). Their ground-state electronic configuration ($S = 5/2$) corresponded to four α-spins in the Mn d-manifold with approximately one α-spin delocalized over the dioxygen moiety (Table 2). Despite this unpaired electron distribution, the NPA charges on Mn of 1.4 computed for models **7** and **8** do not deviate substantially from that observed in complexes **9** and **10**. The NPA charges on the dioxygen moiety sum to −0.38 and −0.50 in the water- and hydroxide-containing models **7** and **8**, respectively. Examination of the α- and β-spin d NBOs for these complexes also shows that approximately 5 electrons are associated with the d-manifold, implying that the formal valence of the metal/dioxygen complex when hydroxide or water are bound in the remaining coordination site corresponds to Mn(II). These results are therefore consistent with a scenario in which dioxygen can bind to Mn(II), with a *net* partial transfer of charge to dioxygen from the ligand sphere. Hence, assuming that such an intermediate $S = 5/2$ spin coupling is feasible at the OxDC active site, dioxygen can associate with the metal to give a complex in which manganese retains divalent d^5 character.[44]

Given that the wave functions computed for the BLYP-optimized active site models were free of spin contamination, we analyzed the d-orbital SMD so as to assign a formal valence to the metal center (Table 2). We generally prefer to employ this measure of valence assignment rather than partial charge values because the latter are not uniquely defined from the wave function and often have limited similarity to the formal charges of transition metal-containing systems.[15e,45]

Mn-Dependent C−C Bond Cleavage

J. Chem. Theory Comput., Vol. 1, No. 5, 2005 **1001**

Table 7. Calculated Covalent Character of Mn−Ligand Bonds in Complexes **7**−**10** at Their BLYP-Optimized Ground-State Geometries[a,b]

bond	bond covalency ($|e^-|$)	total covalency ($|e^-|$)
O_2−H_2O **7** $M_S = 5/2$		
Mn−H95N$^\epsilon$	0.163	0.994
Mn−H97N$^\epsilon$	0.065	
Mn-E101O$^{\delta 1}$	0.322	
Mn−H140N$^\epsilon$	0.125	
Mn−O_A	0.245	
Mn−O_B	0.074	
O_2−HO^- **8** $M_S = 5/2$		
Mn−H95N$^\epsilon$	0.078	1.288
Mn−H97N$^\epsilon$	0.059	
Mn-E101O$^{\delta 1}$	0.192	
Mn−H140N$^\epsilon$	0.125	
Mn−O_A	0.260	
Mn−O_B	0.574	
HO_2−H_2O **9** $M_S = 3/2$		
Mn−H95N$^\epsilon$	0.306	2.193
Mn−H97N$^\epsilon$	0.226	
Mn-E101O$^{\delta 1}$	0.357	
Mn−H140N$^\epsilon$	0.380	
Mn−O_A	0.720	
Mn−O_B	0.204	
HO_2−HO^- **10** $M_S = 3/2$		
Mn−H95N$^\epsilon$	0.262	2.308
Mn−H97N$^\epsilon$	0.178	
Mn−E101O$^{\delta 1}$	0.340	
Mn−H140N$^\epsilon$	0.179	
Mn−O_A	0.656	
Mn−O_B	0.693	

[a] Atom labels correspond to those used in Table 4. [b] M_S is the sum of the Mn and dioxygen spin states.

When applied to the ground-state $S = 3/2$ active site models **9** and **10**, however, SMD analysis suggested that electron transfer had taken place to give Mn(IV) and bound hydroperoxide anion. This was an unexpected finding, especially given that the NPA charges on Mn decreased in complexes **9** and **10** by almost 0.3 electrons (Table 2). We therefore analyzed the extent of metal−ligand covalency in these active site models (Table 7). This analysis showed that the extent of covalency was significantly increased relative to the modest levels seen in the active site models for the resting enzyme (**1**−**3**) and the E-oxalate complex (**4**−**6**). Thus, a total of approximately 1 and 1.3 electrons are shared between the metal and its ligands in complexes **7** and **8**, respectively. The extent of covalency increases further to 2.2 and 2.3 electrons in active site models **9** and **10** (Table 7). As a result, we conclude that SMD quantitation of the formal charge on the metal in the latter complexes is flawed due to a breakdown of the ligand-field approximation associated with high metal−ligand covalency resulting from substantial mixing of the empty Mn *d*-orbital(s) with filled ligand orbitals and thus effective partial electron transfer from the Mn *d*-manifold to the superoxide or peroxide moiety. Thus, rather than Mn(III) or Mn(IV) ligand field complexes, these active site models might be chemically better described

in terms of resonance forms in which oxidized ligands and Mn(II) also participate.

Structural Properties and NBO Analysis of Complexes 11−14 (Dioxygen-Oxalate Reactive Enzyme). We found the effect of binding both oxalate and dioxygen to the manganese center in the OxDC active site models **11**−**14** was critically dependent on the protonation states of these two ligands (Table 8). Thus, when both nonproteinaceous ligands were protonated in model **14**, the length of the BLYP-optimized oxalate C−C bond was 1.56 Å, identical to its value in model **6**, and only 0.01 Å longer than the cognate bond in model **5**, in which water is present in the putative dioxygen binding site. Similarly, the O−O bond length in the hydroperoxy ligand was 1.40 Å, a value slightly shorter than in either of the $S = 3/2$ model complexes **9** and **10**, in which water or hydroxide are bound in the putative oxalate-binding site, respectively. We therefore conclude that when both ligands are protonated, there is no significant perturbation in electronic structure relative to the models in which each is bound separately.

Binding unprotonated dioxygen in oxalate-containing active site models **11** and **12** gave systems for which the lowest energy, ground-state spin multiplicity was 5/2 rather than 3/2, similar to our findings for complexes **7** and **8**, in which water or hydroxide occupy site A, respectively. The O−O distance, however, shortens to 1.28 Å in models **11** and **12**, consistent with a reduction in superoxide or peroxide character (Table 8). The same decrease of approximately 0.1 Å is also observed in complexes **9** and **10** containing the HO_2 ligand (Table 4), suggesting that this behavior arises primarily from local bonding considerations within the dioxygen moiety. Likewise, binding oxalate dianion and dioxygen to give active site model **11** did not have dramatic structural consequences. The bond lengths in the optimized complex **11** were generally longer than those observed in either O_2−OxH **12** or HO_2−OxH **14**, consistent with its overall anionic character (Table 8). It is therefore interesting to note that (i) the Mn−oxalate bond (Mn−O_B) is shorter than the cognate bond in **12**, (ii) the oxalate C−C bond is slightly longer than complexes in which this ligand is protonated, including models **4** and **6**, and (iii) the bond between the ethylimidazole ligand, corresponding to His-95, and the metal is 2.4 Å. The latter distance generally correlated with the overall charge on each model, with protonation of oxalate shortening the bond more than protonation of dioxygen. Simultaneous binding of dioxygen and either oxalate monoanion (**12**) or dianion (**11**) gave BLYP-optimized structures having an $S = 5/2$ ground state that again exhibited only small amounts of spin contamination (Table 2). The NPA charges and SMD on Mn and bound O_2 are consistent with a formal Mn(III) bound to superoxide, as also observed for the dioxygen-containing models **7** and **8**. Some spin magnetization density finds its way onto the oxalate molecule, however, in both the O_2−Ox **11** and O_2−OxH **12** complexes (Table 2). Tellingly, the NPA/NLMO bond order for the oxalate C−C bond is comparable to that computed for the ground-state sextet HO^-−OxH **4** and H_2O−Ox **5** models, although the correlation between oxalate protonation state and C−C bond order appears reversed

Table 8. Selected Structural Properties of BLYP-Optimized Geometries for OxDC Active Site Models **11**−**14**[a]

internal coordinate[b,c]	O_2−Ox **11** $M_S = 5/2$	O_2−OxH **12** $M_S = 5/2$	HO_2−Ox **13** $M_S = 5/2$	HO_2−OxH **14a** $M_S = 3/2$	HO_2−OxH **14b** $M_S = 5/2$
Mn−H95N$^\epsilon$	2.425	2.276	2.326	2.096	2.264
Mn−H97N$^\epsilon$	2.282	2.169	2.327	2.155	2.137
Mn−E101O$^{\delta 1}$	2.123	1.988	2.182	1.952	2.276
Mn−H140N$^\epsilon$	2.236	2.352	2.298	2.092	2.132
Mn−O$_A$	2.096	2.041	1.979	1.860	2.067
Mn−O$_B$	1.986	2.093	2.419	1.894	1.929
C$_A$−C$_B$	1.605	1.561	3.880[d]	1.558	1.558
O$_A$−O$_C$	1.322	1.281	1.509	1.395	1.296
H95N$^\epsilon$−Mn−H97N$^\epsilon$	84.48	89.51	85.85	91.23	91.94
H95N$^\epsilon$−Mn−E101O$^{\delta 1}$	166.6	175.5	163.4	172.4	174.4
H95N$^\epsilon$−Mn−H140N$^\epsilon$	82.98	82.97	86.56	86.41	90.15
H95N$^\epsilon$−Mn−O$_A$	82.76	86.79	89.28	86.33	86.98
H95N$^\epsilon$−Mn−O$_B$	84.58	83.40	103.6	95.03	91.91
H97N$^\epsilon$−Mn−E101O$^{\delta 1}$	85.02	152.3	84.42	85.62	87.45
H97N$^\epsilon$−Mn−H140N$^\epsilon$	88.52	92.29	112.6	93.08	94.30
H97N$^\epsilon$−Mn−O$_A$	166.8	175.2	132.2	177.6	177.9
H97N$^\epsilon$−Mn−O$_B$	92.64	92.61	97.08	88.88	95.70
E101O$^{\delta 1}$−Mn−H140N$^\epsilon$	88.52	93.43	84.77	86.83	84.35
E101O$^{\delta 1}$−Mn−O$_A$	107.1	95.56	107.2	96.83	93.45
E101O$^{\delta 1}$−Mn−O$_B$	104.1	100.4	91.01	91.85	93.69
H140N$^\epsilon$−Mn−O$_A$	86.48	84.20	114.5	87.01	83.94
H140N$^\epsilon$−Mn−O$_B$	167.3	165.5	149.4	177.5	169.7
O$_A$−Mn−O$_B$	89.61	90.03	38.51	91.10	86.11
Mn−O$_A$−O$_C$	115.8	117.1	86.72	120.1	120.4
O$_B$−C$_A$−O$_D$	127.8	130.0	173.8	128.0	128.2
O$_E$−C$_B$−O$_F$	131.6	122.1	179.1	125.3	124.3

[a] All calculations are spin-unrestricted. M_S is the sum of the Mn and dioxygen spin states. [b] All bond distances and angles are reported in units of Å and deg, respectively. [c] O$_A$ and O$_B$ correspond to the ligating oxygen atoms in the buried (site A) and solvent-exposed (site B) coordination sites (Figure 1), respectively, and O$^{\delta 1}$ is the oxygen of the butyrate moiety corresponding to the Glu-101 residue that is bonded directly to the metal. O$_C$ is the atom in dioxygen that is not bound to Mn. C$_A$ and O$_D$ are the remaining atoms in the carboxylate coordinated directly to Mn, and atoms in the other carboxyl moiety in oxalate are defined as C$_B$, O$_E$, and O$_F$. [d] Highlighted internal coordinate is discussed explicitly in the text.

(Table 2). The relationship that oxalate protonation appears to maintain C−C bond order in this ligand, presumably by preventing electron transfer to the Mn center, is still evident when the HO$^-$−OxH **4** and H$_2$O−Ox **5** models are compared with O$_2$−Ox **11** and O$_2$−OxH **12** (Table 2). Finally, the overall metal−ligand covalency in the O$_2$−OxH complex **12** is slightly enhanced relative to that in O$_2$−Ox **11** (Table 9), the majority of the difference arising from enhanced covalency in the bond between the imidazole moiety corresponding to Glu-101 and the metal in **12** being only partially counterbalanced by enhanced metal-O$_2$ covalency in **11**. The addition of a proton to the dioxygen ligand in **12** to give the deprotonated model **14** results in a ground spin multiplicity of $S = 3/2$ based on the lowest energy structure exhibiting modest spin contamination (Table 2). The electronic structure of HO$_2$−OxH **14**, based on the NPA charges and SMD computed for the Mn center and hydroperoxy ligand, resembles the hydroperoxy complexes **9** and **10**. Since the total Mn d-orbital occupancy is 5.5 e$^-$, we consider the metal to be Mn(II) in a quartet state spin state (Table 2). Protonation also increases the oxalate C−C bond order in **14** relative to **12**. Hence, in a result that has important mechanistic implications, merely protonating dioxygen in the OxDC does not appear to be sufficient to weaken the oxalate C−C bond, either by inductive effects or direct electron transfer.

In sharp contrast to the results described above, no stable, minimum energy structure was found for the active site model HO$_2$−Ox **13** in which intact oxalate dianion and protonated dioxygen are both bound to the Mn center. Thus, efforts to optimize **13** using the BLYP functional gave a structure in which the oxalate C−C bond had clearly broken to give two O−C−O fragments with bond angles similar to that in CO$_2$ (Figure 3).[46] Furthermore, the dioxygen ligand becomes bidentate so as to fill the open coordination site produced as a result of C−C bond cleavage, giving Mn−O$_C$ and O$_A$−O$_C$ bond lengths of 1.98 and 1.51 Å, respectively (Table 8). Although it is hard to make any firm mechanistic conclusions in the absence of more detailed reaction path studies,[46] C−C bond cleavage in **13** therefore appears to be correlated with the formation of a Mn-bound peroxide. Notably, the ground spin multiplicity of this complex is 5/2, suggesting that the metal can be formally regarded as Mn(II).
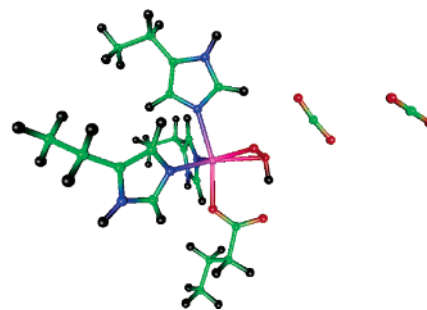
The remarkable finding that C−C bond cleavage occurred in active site model **13** on BLYP optimization led us to investigate whether our choice of model chemistry had been appropriate. The geometries of the model complexes O$_2$−Ox **11**, O$_2$−OxH **12**, HO$_2$−Ox **13**, and HO$_2$−OxH **14** were therefore reoptimized using the B3LYP functional in combination with an SVP(+) basis set. This functional was chosen given (i) its inclusion of orbital-dependent exchange, which tends to stabilize high-spin rather than low-spin

Mn-Dependent C−C Bond Cleavage

J. Chem. Theory Comput., Vol. 1, No. 5, 2005 **1003**

Table 9. Calculated Covalent Character of Mn−Ligand Bonds in Complexes **11**−**14** at Their BLYP-Optimized Ground-State Geometries[a,b]

bond	bond covalency ($|e^-|$)	total covalency ($|e^-|$)
O_2−Ox **11** $M_S = 5/2$		
Mn−H95N$^\epsilon$	0.067	0.872
Mn−H97N$^\epsilon$	0.085	
Mn−E101O$^{\delta 1}$	0.132	
Mn−H140N$^\epsilon$	0.096	
Mn−O$_A$	0.319	
Mn−O$_B$	0.173	
O_2−OxH **12** $M_S = 5/2$		
Mn−H95N$^\epsilon$	0.103	0.927
Mn−H97N$^\epsilon$	0.125	
Mn−E101O$^{\delta 1}$	0.244	
Mn−H140N$^\epsilon$	0.083	
Mn−O$_A$	0.234	
Mn−O$_B$	0.138	
HO_2−Ox **13** $M_S = 5/2$		
Mn−H95N$^\epsilon$	0.072	0.682
Mn−H97N$^\epsilon$	0.078	
Mn−E101O$^{\delta 1}$	0.108	
Mn−H140N$^\epsilon$	0.083	
Mn−O$_A$	0.277	
Mn−O$_C$	0.064[c]	
HO_2−OxH **14a** $M_S = 3/2$		
Mn−H95N$^\epsilon$	0.256	2.058
Mn−H97N$^\epsilon$	0.176	
Mn−E101O$^{\delta 1}$	0.472	
Mn−H140N$^\epsilon$	0.122	
Mn−O$_A$	0.664	
Mn−O$_B$	0.368	
HO_2−OxH **14b** $M_S = 5/2$		
Mn−H95N$^\epsilon$	0.128	1.163
Mn−H97N$^\epsilon$	0.154	
Mn−E101O$^{\delta 1}$	0.080[d]	
Mn−H140N$^\epsilon$	0.168	
Mn−O$_A$	0.374[d]	
Mn−O$_B$	0.259	

[a] Atom labels correspond to those used in Table 4. [b] M_S is the sum of the Mn and dioxygen spin states. [c] Optimization resulted in C−C bond cleavage to generate two dissociated molecules of carbon dioxide. The coordinating ligand in site B was therefore the protonated oxygen atom (O$_C$) of the hydroperoxide anion formed by electron transfer (Figure 3). [d] Optimization resulted in transfer of a proton from the hydroperoxide ligand to the O$^{\delta 1}$ oxygen of the butyrate moiety corresponding to Glu-101 (*Bacillus subtilis* numbering). This likely reflects the greater charge on the carboxylate oxygens versus O_2 in the $M_S = 5/2$ complex. Notably, all complexes with protonated dioxygen in $M_S = 3/2$ complexes did not show such a transfer, suggesting that the low-spin coupling (physically between $S = 5/2$ high-spin Mn and $S = 1$ dioxygen) promotes electron transfer to the O_2 moiety. This is consistent with Pauli exclusion and implies that dioxygen protonation will not occur prior to oxalate deprotonation.

Figure 3. Low-energy structure of the HO_2−Ox active site model complex at $M_S = 5/2$ spin multiplicity, showing C−C bond scission to yield two CO_2 molecules and a hydroperoxide ligand. Atoms are colored using the following scheme: C, green; H, black; N, blue; O, red; Mn, magenta.

the B3LYP functional was used to optimize model **13**, the C−C bond in the oxalate ligand elongated to over 1.88 Å, an observation clearly consistent with significant weakening even though complete dissociation did not occur. Presumably, this difference arises from the description of exchange in BLYP (a pure functional) and B3LYP (a hybrid functional with some explicit orbital-dependent exchange) involving orbitals centered on each oxalate-CO_2^δ- fragment. Similarly, the dioxygen O_A−O_C bond elongated to 1.43 Å, rather than 1.51 Å as seen in the BLYP-optimization. Model complexes **11**, **12**, and **14**, however, showed no significant differences in the optimized geometries obtained in calculations employing either BLYP or B3LYP functionals.

In addition to the geometric changes that take place during BLYP optimization of the HO_2−Ox complex **13**, substantial reorganization of the electronic structure occurs when dioxygen is protonated and oxalate deprotonated. The ground state of this complex is a spin sextet, which deviates from the behavior of the analogous HO_2−H_2O and HO_2−HO complexes, both of which were ground-state quartets. Although the NPA charge on Mn is unremarkable compared to that in complexes, **11**, **12**, and **14**, the charges on both atoms of dioxygen in **13** are noticeably lower than in any other dioxygen-containing model examined in these studies (Table 2). Perhaps more significantly, the SMD of the Mn ion in the final structure of **13** suggests that the manganese is best considered as divalent, which is consistent with an overall metal−ligand covalency of 0.68 $|e^-|$, lower than that observed for dioxygen-containing models **4**−**6**, **12**, and **14**, and even the HO−H_2O resting complex **3**. Overall, simultaneous O_2 protonation and deprotonation of oxalate therefore results in an apparent ligand oxidation to give a complex in which Mn(II) is bound to hydroperoxide (Figure 3). Thus, even the truncated models considered here exhibit chemistry that is essentially that of the manganese center in oxalate oxidase.

Mechanistic Relevance. Several mechanistically interesting points can be inferred from these model calculations. First, C−C bond cleavage in Mn-bound oxalate with concomitant oxidation of the substrate and dioxygen reduction requires both the formation of an oxalate anion *and* polarization of the dioxygen-derived ligand. Although we model the latter requirement in these calculations by the

multiplicities due to stabilization of parallel spins by Fermi exchange,[47] and (ii) its excellent performance when used with basis sets of modest size.[48] In addition, all optimizations were carried out for $M_S = 5/2$, in part because this configuration is expected to maximize Pauli repulsion and hence disfavor electron redistribution from oxalate to the HO_2 moiety, thereby biasing the calculation against oxidation. Even when

addition of a proton to form a Mn-bound hydroperoxy species in complexes **13** and **14**, examination of the crystal structure of *Bacillus subtilis* OxDC does not show any residues that might function as general acids to accomplish such a protonation. It is therefore likely that if dioxygen indeed coordinates the active site Mn, electrostatic polarization of the O−O bond would have to result from the protein environment surrounding the metal center. Modulation of the extent of such polarization might be a potential means to discriminate between oxalate decarboxylation and oxidation, which we have suggested differ by the transfer of one or two electrons from oxalate to metal-bound dioxygen, respectively. Second, the need to deprotonate the distal carboxylic acid of the oxalate substrate is consistent with experimental proposals that rationalize observed kinetic isotope effects,[9] and the functional importance of Glu-162, which is an excellent candidate for the general base on the basis of site-directed mutagenesis studies.[17] On this point, we note that mutation of this residue to alanine results in an E162A OxDC mutant that exhibits oxalate oxidase rather than decarboxylase activity. This interesting observation can be rationalized on the basis of these calculations by postulating direct proton transfer from Mn-bound oxalate to the dioxygen-derived ligand in an adjacent coordination site as a consequence of greater conformational freedom and the absence of the general base to yield an intermediate similar to **13** with subsequent C−C bond cleavage and electron transfer to form two molecules of CO_2. In the presence of Glu-162, however, hydrogen bonding between the distal end of bound oxalate monoanion and the Glu-162 protein side chain, together with the absence of a proton donor in the hydrophobic pocket to which we suggest dioxygen binds, would prevent such a proton transfer thereby preventing substrate oxidation and favoring decarboxylation to yield a formal metal-bound formyl radical anion (Scheme 1). Verification or refutation of this idea awaits further experimental and computational study.

Conclusions

All mechanistic proposals for OxDC to date have postulated the involvement of formal oxidation states for manganese that are higher than that observed (Mn(II)) in the resting enzyme by electron paramagnetic resonance spectroscopy.[2a,9,11] In part, these hypotheses reflect the need to rationalize (i) the generation of an oxalate radical anion as an intermediate and (ii) the requirement of the enzyme for oxygen during catalytic turnover.[2a] This conflicts, however, with the total Mn *d*-orbital occupancy of slightly more than five electrons that is a common element of all the ground-state structures computed in this study. In the case of active site models **1−6**, this electronic configuration can be explained from simple ligand field theory, i.e., that Mn(II) is coordinated by relatively inert ligands that transfer a small amount of charge into the empty Mn 4*s* orbital to form stable complexes. In the other cases, such as **7−14**, in which some form of dioxygen is bound to the metal, divalency arises instead from the presence of bonds with significant covalency that are formed by extensive mixing of atomic orbitals on Mn (*d*) and ligand atoms (*s,p*) to give molecular orbitals with

significant Mn *d* character. One might think of this in terms of ligand redox noninnocence,[49] i.e., there is effectively partial electron transfer to the metal ion. Thus, although any assignment of formal or spectroscopic oxidation state in the latter models is complicated by the nature of the metal−ligand bonding,[49a,50] if such a state is demanded our calculations suggest that Mn(II) persists even when the metal is bound to oxidizing species, such as dioxygen or hydroperoxide radical. Our results therefore raise the possibility that the Mn(II) center may play an alternative role in the OxOx and OxDC-mediated cleavage of the oxalate C−C bond. Such a proposal is also consistent with recent failures to observe Mn(III)-containing species when OxDC is undergoing steady-state turnover.[3b]

Thus, the function of the metal ion may be to juxtapose dioxygen and oxalate, or formate radical anion (its breakdown product), and establish an electronic structure such that electrons can be shuttled directly between these species, thereby removing the need for the existence of Mn(III) as a discrete intermediate oxidant that would be formed by metal-to-dioxygen charge transfer. In a mechanism in which divalent manganese serves as a mediator, active site models **12−14** are particularly intriguing. In models **12** and **14** the oxalate C−C bond order is approximately 0.9 (Table 2), and there is a small amount of electron transfer from Mn(II) to the bound form of dioxygen. Removal of a proton from oxalate, however, yields a model (**13**) for which no stable minimum containing an intact oxalate C−C bond is obtained upon geometry optimization, at least in the absence of solvation, perhaps implying that the intrinsic reactivity of the active center in *Bacillus subtilis* oxalate *decarboxylase* is to *oxidize* oxalate. Although it might be argued that this result reflects a poor choice of functional, the behavior of this active site model when optimization was performed using B3LYP, which includes a significant amount of orbital-dependent exchange, was qualitatively consistent. While the change of exchange functional yielded a structure containing an oxalate C−C bond, once again the presence of oxalate anion and the hydroperoxy ligand in model **13** resulted in a significant weakening of this bond. Thus, we tentatively conclude that the intrinsic reactivity of the Mn(II) center is to promote proton-coupled electron transfer from oxalate to protonated dioxygen to form a metal-bound peroxide anion.

Since this intrinsic reactivity is not observed in OxDC, we believe that these calculations provide evidence to support the hypothesis that OxDC evolved from OxOx by gene duplication leading to a bicupin structure in which the protein environment modulates the intrinsic metallocenter reactivity.[51] The overall cupin fold around the metallocenter is largely unchanged by this hypothetical duplication, so our finding that a common intrinsic reactivity for the manganese centers in the two enzymes in the absence of a detailed description of their polypeptide surroundings is not too surprising. The different transformations of oxalate that are catalyzed by OxOx and OxDC may therefore reflect subtle changes in electrostatics, hydrogen bonding, and differential molecular dynamics associated with the protein structure in which the metal center is embedded. One plausible scenario is that mutations close to the manganese center in OxDC

Mn-Dependent C−C Bond Cleavage

J. Chem. Theory Comput., Vol. 1, No. 5, 2005 **1005**

have accumulated to ensure that (i) manganese-bound dioxygen cannot be protonated and/or (ii) the intermediate formate radical anion is protonated prior to transfer of a second electron to the Mn-superoxyl system, which would presumably be coupled to flattening of the O−C−O bond angle in the formyl radical.[52] In this regard, it is interesting to note that the removal of one metal binding site in OxDC by site-directed mutagenesis largely eliminates the catalytic activity of the other site,[53] raising the intriguing possibility that the two sites in the enzyme may be redox-coupled. Regardless of whether such intersite communication holds up to experimental scrutiny,[17] the molecular basis for the apparent evolutionary honing of OxOx to OxDC reactivity remains to be elucidated.

Supporting Information Available: Complete citation for ref 34 and Cartesian coordinates for the B3LYP-optimized structures of models **11**−**13** and **14b**. This material is available free of charge via the Internet at http://pubs.acs.org.

References

(1) (a) Dutton, M. V.; Kathiara, M.; Gallagher, I. M.; Evans, C. S. *FEMS Microbiol. Lett.* **1994**, *116*, 321−326. (b) Magro, P.; Marciano, P.; Di Lenna, P. *FEMS Microbiol. Lett.* **1988**, *49*, 49−52. (c) Lillehoj, E. B.; Smith, F. G. *Arch. Biochem. Biophys.* **1965**, *109*, 216−220. (d) Shimazono, H.; Hayaishi, O. *J. Biol. Chem.* **1957**, *227*, 151−159. (e) Shimazono, H. *J. Biochem. (Tokyo)* **1955**, *42*, 321−340.

(2) (a) Tanner, A.; Bowater, L.; Fairhurst, S. A.; Bornemann, S. *J. Biol. Chem.* **2001**, *276*, 43627−43634. (b) Tanner, A.; Bornemann, S. *J. Bacteriol.* **2000**, *182*, 5271−5273.

(3) (a) Svedružić, D.; Jónsson, S.; Toyota, C. G.; Reinhardt, L. A.; Ricagno, S.; Lindqvist, Y.; Richards, N. G. J. *Arch. Biochem. Biophys.* **2005**, *433*, 176−192. (b) Chang, C. H.; Svedružić, D.; Ozarowski, A.; Yeagle, G.; Walker, L.; Britt, R. D.; Angerhofer, A.; Richards, N. G. J. *J. Biol. Chem.* **2004**, *279*, 52840−52849.

(4) (a) Emiliani, E.; Riera, B. *Biochim. Biophys. Acta* **1968**, *167*, 414−421. (b) Emiliani, E.; Bekes, P. *Arch. Biochem. Biophys.* **1964**, *105*, 488−493.

(5) (a) Borodine, A. *Annalen* **1861**, *119*, 121−123. (b) Kolbe, H. *Annalen* **1849**, *69*, 257−294.

(6) Hunsdiecker, H.; Hunsdiecker, C. *Chem. Ber.* **1942**, *75*, 291−297.

(7) Halliwell, B. *Biochem. J.* **1972**, *129*, 497−498.

(8) Drummond, A. Y.; Waters, W. A. *J. Chem. Soc.* **1953**, 435−443.

(9) Reinhardt, L. A.; Svedruzic, D.; Chang, C. H.; Cleland, W. W.; Richards, N. G. J. *J. Am. Chem. Soc.* **2003**, *125*, 1244−1252.

(10) (a) Huynh, M. H. V.; Meyer, T. J. *Proc. Natl. Acad. Sci. U.S.A.* **2004**, *101*, 13138−13141. (b) Qu, S. J.; Klinman, J. P. *Biochemistry* **1998**, *37*, 12513−12525.

(11) Anand, R.; Dorrestein, P. C.; Kinsland, C.; Begley, T. P.; Ealick, S. E. *Biochemistry* **2002**, *41*, 7659−7669.

(12) Koch, W.; Holthausen, M. C. *A Chemist's Guide to Density Functional Theory*, 2nd ed.; Wiley-VCH: Weinheim, 2001. (b) Siegbahn, P. E. M.; Blomberg, M. R. A. *Annu. Rev. Phys. Chem.* **1999**, *50*, 221−249. (c) Siegbahn, P. E. M. *Adv. Chem. Phys.* **1996**, *93*, 333−387.

(13) (a) Weinhold, F. In *Encyclopedia of Computational Chemistry*; Schleyer, P. v. R., Allinger, N. L., Clark, T., Gasteiger, J., Kollman, P. A., Schaefer III, H. F., Schreiner, P. R., Eds.; Wiley: Chichester, 1998; pp 1792−1811. (b) Reed, A. E.; Curtiss, L. A.; Weinhold, F. *Chem. Rev.* **1988**, *88*, 899−926.

(14) Fe-dependent enzymes: (a) Solomon, E. I.; Szilagyi, R. K.; DeBeer George, S.; Basumallick, L. *Chem. Rev.* **2004**, *104*, 419−458. (b) Bassan, A.; Borowski, T.; Siegbahn, P. E. M. *J. Phys. Chem. B* **2004**, *108*, 13031−13041. (c) Boone, A. J.; Chang, C. H.; Greene, S. N.; Herz, T.; Richards, N. G. J. *Coord. Chem. Rev.* **2003**, *238−239*, 291−314. (d) Friesner, R. A.; Baik, M. H.; Gherman, B. F.; Guallar, V.; Wirstam, M.; Murphy, R. B.; Lippard, S. J. *Coord. Chem. Rev.* **2003**, *238−239*, 267−290. (e) Ghosh, A.; Steene, E. *J. Biol. Inorg. Chem.* **2001**, *6*, 739−752. (f) Harris, D. L. *Curr. Opin. Chem. Biol.* **2001**, *5*, 724−735. (g) Spiro, T. G.; Zgierski, M. Z.; Kozlowski, P. M. *Coord. Chem. Rev.* **2001**, *219−221*, 923−936. (h) Li, S.; Hall, M. B. *Inorg. Chem.* **2001**, *40*, 18−24. (i) Siegbahn, P. E. M.; Blomberg, M. R. A. *Chem. Rev.* **2000**, *100*, 421−437.

(15) Mn-dependent enzymes: (a) Noodleman, L.; Lovell, T.; Han, W. G.; Himo, F. *Chem. Rev.* **2004**, *104*, 459−508. (b) Sinnecker, S.; Neese, F.; Noodleman, L.; Lubitz, W. *J. Am. Chem. Soc.* **2004**, *126*, 2613−2622. (c) Ivanov, I.; Klein, M. L. *Proteins: Struct. Funct. Genet.* **2003**, *54*, 1−7. (d) Himo, F.; Siegbahn, P. E. M. *Chem. Rev.* **2003**, *103*, 2421−2456. (e) Siegbahn, P. E. M. *Curr. Opin. Chem. Biol.* **2002**, *6*, 227−235. (f) Siegbahn, P. E. M. *Theor. Chem. Acc.* **2001**, *105*, 197−206.

(16) Berman, H. M.; Westbrook, J.; Feng, Z.; Gilliland, G.; Bhat, T. N.; Weissig, H.; Shindyalov, I. N.; Bourne, P. B. *Nucl. Acids Res.* **2000**, *28*, 235−242.

(17) Just, V. J.; Stevenson, C. E. M.; Bowater, L.; Tanner, A.; Bornemann, S. *J. Biol. Chem.* **2004**, *279*, 19867−19874.

(18) In structural comparisons, active site models were super-imposed by overlapping the constrained methyl carbons using algorithms implemented in a custom Python script, which employed the following freely available supplementary modules: Numerical Python (Dubois, P. F. available on the World Wide Web at http://sourceforge.net/projects/numpy as of January 2005) and Scientific Python (Hinson K. module library available on the World Wide Web at http://starship.python.net/~hinsen/ScientificPython/ as of January 2005). This script and/or the Cartesian coordinates for the initial and optimized structures of active site models **1**−**14** can be obtained from the authors on request.

(19) (a) Von Arnim, M.; Ahlrichs, R. *J. Comput. Chem.* **1998**, *19*, 1746−1757. (b) Ahlrichs, R.; Bär, M.; Häser, M.; Horn, H.; Kölmel, C. *Chem. Phys. Lett.* **1989**, *162*, 165−169.

(20) (a) Becke, A. D. *J. Chem. Phys.* **1993**, *98*, 5648−5652. (b) Lee, C.; Yang, W.; Parr, R. G. *Phys. Rev. B* **1988**, *37*, 785−789.

(21) Schäfer, A.; Horn, H.; Ahlrichs, R. *J. Chem. Phys.* **1992**, *97*, 2571−2577.

(22) (a) Eichkorn, K.; Weigend, F.; Treutler, O.; Ahlrichs, R. *Theor. Chem. Acc.* **1997**, *97*, 119−124. (b) Eichkorn, K.; Treutler, O.; Öhm, H.; Häser, M.; Ahlrichs, R. *Chem. Phys. Lett.* **1995**, *240*, 283−290. (c) Neese, F.; Olbrich, G. *Chem. Phys. Lett.* **2002**, *362*, 170−178.

(23) (a) Clark, T.; Chandrasekhar, J.; Spitznagel, G. W.; Schleyer, P. v. R. *J. Comput. Chem.* **1983**, *4*, 294−301. (b) Hariharan, P. C.; Pople, J. A. *Theor. Chim. Acta* **1973**, *28*, 213−222. (c) Hehre, W. J.; Ditchfield, R.; Pople, J. A. *J. Chem. Phys.* **1972**, *56*, 2257−2261.

(24) We note that the implementation of B3LYP within TURBOMOLE differs from the standard form implemented in Gaussian,[25] in that the fifth (VWN-V) rather than the third (VWN-III) form of the VWN local correlation is employed.[26]

(25) Stephens, P. J.; Devlin, F. J.; Chabalowski, C. F.; Frisch, M. J. *J. Phys. Chem.* **1994**, *98*, 11623−11627.

(26) Vosko, S. H.; Wilk, L.; Nusair, M. *Can. J. Chem.* **1980**, *58*, 1200−1211.

(27) Hay, P. J.; Wadt, W. R. *J. Chem. Phys.* **1985**, *82*, 299−310.

(28) (a) Chang, C. H.; Boone, A. J.; Bartlett, R. J.; Richards, N. G. J. *Inorg. Chem.* **2004**, *43*, 458−472. (b) Greene, S. N.; Richards, N. G. J. *Inorg. Chem.* **2004**, *43*, 7030−7041.

(29) Reed, A. E.; Weinhold, F. *J. Chem. Phys.* **1985**, *83*, 1736−1740.

(30) Reed, A. E.; Weinstock, R. B.; Weinhold, F. *J. Chem. Phys.* **1985**, *83*, 735−746.

(31) Reed, G. H.; Markham, G. D. In *Biological Magnetic Resonance*; Berliner, L. J., Reuben, J., Eds.; Plenum Press: New York, 1984; Vol. 6, pp 73−142.

(32) Baes, C. F., Jr.; Mesmer, R. E. *The Hydrolysis of Cations*; Wiley-Interscience: New York, 1976.

(33) For example, the oxalate moiety cleaved to give two CO_2 molecules when a dianionic $HO^−$−ox active site model structure was optimized within the RI approximation using a basis that lacked diffuse functions. When the same complex was optimized without this Coulomb integral approximation, its behavior was similar to that observed for the $HO^−$−OxH complex **4** in that the ethylimidazole ligands corresponding to His-95 and His-140 merely dissociated from the metal center. Given these radically different results, we attribute the apparent oxalate oxidation in the RI-BLYP/SVP calculation to spurious "electron transfer" from dianionic oxalate to the metal complex. Such observations are clearly the result of an inadequate description of these strongly charged species in vacuo, an interpretation supported by occupation of positive-energy molecular orbitals even in the calculations including diffuse functions. The latter is a hallmark of either a lack of sufficiently diffuse basis functions which would allow proper description of a (marginally) stable anion in vacuo or a lack of continuum basis functions which would permit a description of the ionization that would actually occur physically in vacuo.

(34) Schwarzenbacher, R. et al. *Proteins: Struct. Funct. Genet.* **2004**, *56*, 392−395.

(35) (a) Coleman, W. M.; Taylor, L. T. *Coord. Chem. Rev.* **1980**, *32*, 1−31. (b) Que, L.; Reynolds, M. F. *Met. Ions Biol. Syst.* **2000**, *37*, 505−525. (c) Vetting, M. W.; Wackett, L. P.; Que, L.; Lipscomb, J. D.; Ohlendorf, D. H. *J. Bacteriol.* **2004**, *186*, 1945−1958.

(36) (a) Mills, S. A.; Klinman, J. P. *J. Am. Chem. Soc.* **2000**, *122*, 9897−9904. (b) Qu, S. J.; Klinman, J. P. *Biochemistry* **1998**, *37*, 8572−8581.

(37) (a) Metz, M.; Solomon, E. I. *J. Am. Chem. Soc.* **2001**, *123*, 4938−4950. (b) Brunold, T. C.; Solomon, E. I. *J. Am. Chem. Soc.* **1999**, *121*, 8288−8295.

(38) (a) van Gastel, M.; Lubitz, W.; Lassmann, G.; Neese, F. *J. Am. Chem. Soc.* **2004**, *126*, 2237−2246. (b) Witting, P. K.; Mauk, A. G. *J. Biol. Chem.* **2001**, *276*, 16540−16547. (c) Licht, S.; Gerfen, G. J.; Stubbe, J. *Science* **1996**, *271*, 477−481. (d) Balagopalakrishna, C.; Abugo, O. O.; Horsky, J.; Manoharan, P. T.; Nagababu, E.; Rifkind, J. M. *Biochemistry* **1998**, *37*, 13194−13202. (e) Cadenas, E. *Methods Enzymol.* **1995**, *251*, 106−116. (f) McEldoon, J. P.; Dordick, J. S. *J. Biol. Chem.* **1989**, *266*, 14288−14293.

(39) (a) Schlichting, I.; Berendzen, J.; Chu, K.; Stock, A. M.; Mayes, S. A.; Benson, D. E.; Sweet, B. M.; Ringe, D.; Petsko, G. A.; Sligar, S. G. *Science* **2000**, *287*, 1615−1622. (b) Gouet, P.; Jouve, H. M.; Williams, P. A.; Anderson, I.; Andreoletti, P.; Nussaume, L.; Hadju, J. *Nat. Struct. Biol.* **1996**, *3*, 951−956. (c) Ghosh, A. K.; Steene, E. *J. Biol. Inorg. Chem.* **2001**, *6*, 739−752. (d) Fabian, M.; Palmer, G. *Biochemistry* **2001**, *40*, 1867−1874.

(40) (a) Fouqueau, A.; Mer, S.; Casida, M. E.; Daku, L. M. L.; Hauser, A.; Mineva, T.; Neese, F. *J. Chem. Phys.* **2004**, *120*, 9473−9486. (b) Swart, M.; Groenhof, A. R.; Ehlers, A. W.; Lammertsma, K. *J. Phys. Chem. A* **2004**, *108*, 5479−5483. (c) Ghosh, P.; Bill, E.; Weyhermuller, T.; Neese, F.; Wieghardt, K. *J. Am. Chem. Soc.* **2003**, *125*, 1293−1308. (d) Staroverov, V. N.; Davidson, E. R. *Chem. Phys. Lett.* **2001**, *340*, 142−150.

(41) (a) Gräfenstein, J.; Cremer, D. *Mol. Phys.* **2001**, *99*, 981−989. (b) Wang, J.; Becke, A. D.; Smith, V. H., Jr. *J. Chem. Phys.* **1995**, *102*, 3477−3480. (c) Baker, J.; Scheiner, A.; Andzelm, J. *Chem. Phys. Lett.* **1993**, *216*, 380−388.

(42) (a) Noodleman, L.; Peng, C. Y.; Case, D. A.; Mouesca, J.-M. *Coord. Chem. Rev.* **1995**, *144*, 199−244. (b) Noodleman, L.; Case, D. A. *Adv. Inorg. Chem.* **1992**, *38*, 423−470. (c) Noodleman, L.; Case, D. A.; Aizman, A. *J. Am. Chem. Soc.* **1988**, *110*, 1001−1005.

(43) (a) Yoo, S. J.; Angove, H. C.; Burgess, B. K.; Hendrich, M. P.; Münck, E. *J. Am. Chem. Soc.* **1999**, *121*, 2534−2545. (b) Papaefthymiou, V.; Millar, M. M.; Münck, E. *Inorg. Chem.* **1986**, *25*, 3010−3014.

(44) Such a model is by definition oversimplified given the covalency of bonding and consequent breakdown of the ligand field approximation. It is nevertheless useful to frame the discussion of the formal valence of the manganese ion within that given in the literature.

(45) The discrepancy between formal and partial charge in first-row transition ions often arises as a result of charge transfer from the ligand into the metal 4*s* orbital associated with coordinate-covalent bonding.

(46) The geometry optimization of complexes for which oxalate C−C bond cleavage occurs is partial, given the difficulty of locating a well-defined minimum energy structure due to flattening of the potential surface. In any event, oxalate C−C bond clearly breaks, and the linear O−C−O angles strongly suggest that the observed "cleavage" is oxidative. While recognizing that it is technically fallacious to discuss changes during a geometry optimization in terms of a chemical reaction, these changes nevertheless imply that a stable,

Mn-Dependent C−C Bond Cleavage

J. Chem. Theory Comput., Vol. 1, No. 5, 2005 **1007**

minimum-energy structure in which the oxalate C−C bond is intact was not be found with this model chemistry, starting geometry, and gradient and Hessian update algorithms. We have therefore framed our discussion of the behavior of model complex **13** relative to that of other *minimized* structures obtained in these studies.

(47) (a) Salomon, O.; Reiher, M.; Hess, B. A. *J. Chem. Phys.* **2002**, *117*, 4729−4737. (b) Reiher, M.; Salomon, O.; Hess, B. A. *Theor. Chem. Acc.* **2001**, *107*, 48−55.

(48) This performance enhancement has been suggested to arise from a fortuitous cancellation of errors between truncated bases and the erroneous long-range behavior of the exchange-correlation potential (see ref 12).

(49) (a) Bill, E.; Bothe, E.; Chaudhuri, P.; Chlopek, K.; Herebian, D.; Kokatam, S.; Ray, K.; Weyhermüller, T.; Neese, F.; Wieghardt, K. *Chem. Eur. J.* **2005**, *11*, 204−224. (b) Chaudhuri, P.; Verani, C. N.; Bill, E.; Bothe, E.; Weyhermüller, T.; Neese, F.; Wieghardt, K. *J. Am. Chem. Soc.* **2001**, *123*, 2213−2223.

(50) Jörgensen, C. K. *Oxidation Numbers and Oxidation States*; Springer: Berlin, 1969.

(51) (a) Dunwell, J. M.; Khuri, S.; Gane, P. J. *Microbiol. Mol. Biol. Rev.* **2000**, *64*, 153−179. (b) Dunwell, J. M.; Culham, A.; Carter, C. E.; Sosa-Aguirre, C. R.; Goodenough, P. W. *Trends Biochem. Sci.* **2001**, *26*, 740−745.

(52) (a) Krauss, M.; Neumann, D. *Chem. Phys. Lett.* **1972**, *14*, 26−27. (b) Pacansky, J.; Wahlgren, U.; Bagus, P. S. *J. Chem. Phys.* **1975**, *62*, 2740−2744.

(53) Chakraborty, S.; Chakraborty, N.; Jain, D.; Salunke, D. M.; Datta, A. *Protein Sci.* **2002**, *11*, 2138−2147.